Oceanic redox evolution around the end-Permian mass extinction at Meishan, South China

Lei Xiang[a], Hua Zhang[a,*], Shane D. Schoepfer[b], Chang-qun Cao[a], Quan-feng Zheng[a], Dong-xun Yuan[a], Yao-feng Cai[a], Shu-zhong Shen[c]

[a] State Key Laboratory of Palaeobiology and Stratigraphy, Nanjing Institute of Geology and Palaeontology, Center for Excellence in Life and Paleoenvironment, Chinese Academy of Sciences, 39 East Beijing Road, Nanjing 210008, China
[b] Department of Geosciences and Natural Resources, Western Carolina University, 1 University Way, Cullowhee, NC 28779, USA
[c] School of Earth Sciences and Engineering, Nanjing University, 163 Xianlin Avenue, Nanjing 210023, China

ARTICLE INFO

ABSTRACT

The end-Permian marine extinction (EPME) eliminated > 80% of species globally, making it the most severe extinction of the Phanerozoic. Anoxia and euxinia are potential kill mechanisms that may have contributed to this biotic crisis. However, redox changes in the atmosphere-ocean system are likely to have been complex, with both the vertical location of the oxic-anoxic boundary (in the water column or sediments), and the total area or volume of anoxic and euxinic water in the global ocean changing over time. In this study, we generated iron speciation and major and trace element data from 141 samples of the Meishan-1 core, which was drilled at a site 550 m to the west of the Meishan D section. Iron speciation results, in combination with authigenic concentrations and enrichment factors of redox-sensitive metals (Mo, V, and U), and previously published macro-fossil, trace fossil, and bioturbation evidence, suggest that: 1) Beds 21-24d were deposited beneath a predominantly oxic water column, 2) Beds 24e-28 were deposited under a persistently anoxic watermass with intermittently euxinic bottom water, and 3) Beds 29–34 were deposited under primarily ferruginous conditions. Excess fractions and enrichment factors of U, V and Mo in the anoxic and euxinic intervals of the Meishan-1 core suggest that authigenic precipitation of redox-sensitive trace metals mainly occurred before and during the EPME, with nearly no detectable authigenic U, V, or Mo accumulating after the EPME. Our results, along with published U, V and Mo concentrations from across the Neotethys, Paleotethys, and Panthalassic Ocean basins, indicate that oceanic trace metal reservoirs were depleted before and during the main extinction interval. This depletion of oceanic trace elements suggests a spatial expansion of both anoxic and euxinic watermasses prior to and during the EPME. The apparent coincidence in timing between the mass extinction and the areal expansion of anoxic and euxinic watermasses suggests that these factors played important roles in the loss of marine biota around the Permian-Triassic boundary (PTB), through oxygen deprivation and H₂S toxicity.

1. Introduction

The end-Permian mass extinction (EPME) was the most severe biodiversity crisis of the last 541 Myr, and is estimated to have eliminated > 80% of marine species (Sepkoski, 1984; Stanley, 2016). Many potential triggers and kill mechanisms have been proposed over the past few decades, such as an extraterrestrial impact (Basu et al., 2003; Becker et al., 2001), Siberian Traps volcanism (Courtillot and Renne, 2003; Sobolev et al., 2011; Burgess and Bowring, 2015); rapid global warming (Joachimski et al., 2012; Sun et al., 2012; Chen et al., 2016; H. J. Song et al., 2014), metal poisoning (Grasby et al., 2011, 2017; Wang et al., 2018), oceanic acidification and acid rain (Black et al., 2014,

2018; Payne et al., 2010; Hinojosa et al., 2012; Clarkson et al., 2015; Garbelli et al., 2017), rapid enhancement of continental weathering (Algeo and Twitchett, 2010; Song et al., 2015; Sun et al., 2018; Tian et al., 2019), and oceanic anoxia/euxinia (Wignall and Twitchett, 1996; Isozaki, 1997; Cao et al., 2009; Grice et al., 2005; Penn et al., 2018; Y.A. Shen et al., 2011; H. J. Song et al., 2014; H. Y. Song et al., 2014a).

A marine 'superanoxic' event around the Permian-Triassic transition was first proposed over two decades ago (Wignall and Twitchett, 1996; Isozaki, 1997). While the atmospheric partial pressure of O₂ (pO₂) may have declined around the PTB, its absolute value probably remained > 17% (Huey and Ward, 2005; W.J. Shen et al., 2011). As a result, those parts of the shallow ocean in regular contact with the

---

atmosphere are likely to have remained oxygenated. The spatial and temporal extent of anoxia in the deeper ocean has remained controversial. The location of the oxic-anoxic boundary (chemocline), whether in the oceanic water column or sediment porewater system, is likely to have been dynamic throughout the PTB interval (Clarkson et al., 2016; Grasby and Beauchamp, 2009; Grasby et al., 2013, 2016). Rapid variation in the sulfur isotope composition of carbonate-associated sulfate suggests a drawdown of the oceanic sulfate reservoir around the PTB, which was likely driven by accelerated microbial sulfate reduction (MSR) under widespread anoxic conditions (Newton et al., 2004; Cao et al., 2009; Luo et al., 2010; H. Y. Song et al., 2014b). The production of H_2S via MSR (and the exsolution of that H_2S into the atmosphere) has been proposed as a potential kill mechanism for the EPME (Kump et al., 2005). However, whether stoichiometric relationships between H_2S production via MSR and its removal in the form of insoluble metal sulfides was sufficient to quantitatively sequester dissolved transition metal ions, such as dissolved ferrous Fe (Fe^{2+}), and thus drive the ocean into a pervasively euxinic rather than ferruginous state, remains the subject of debate (Grice et al., 2005; Kump et al., 2005; Mettam et al., 2017).

The speciation of iron in sedimentary rocks is a widely-used proxy for O_2 and H_2S availability in the depositional watermass (Raiswell et al., 2018). Since the Meishan section, the Global Stratotype Section and Point (GSSP) of the PTB, is one of the most thoroughly investigated EPME sections worldwide (Jin et al., 2000; Yin et al., 1996, 2001, 2012; Wang et al., 2014; S.Z. Shen et al., 2011; Burgess et al., 2014), it is an ideal location to employ iron speciation and redox sensitive trace metal proxies, in order to explore the evolution of redox conditions and their temporal relationship with the EPME. However, the extinction interval at Meishan is highly condensed (36 cm), meaning that the temporal resolution of geochemical studies is limited by the difficulties of outcrop sampling (Shen et al., 2019). In this study, we conducted high-resolution sampling of the Meishan-1 core, drilled less than 1 km from the GSSP section. After sampling the extinction interval in detail, we analyzed iron speciation and major and trace element content in order to reconstruct the evolution of redox conditions and their implications for the EPME.

2. Geological setting

The Meishan section is located in the town of Meishan, Changxing County, Zhejiang Province (119°41′52.80″E, 31°4′36.74″N, Fig. 1). The section represents a shallow upper slope environment, on the margin of the intracratonic carbonate platform that made up the majority of the South China microcontinent during the Permian-Triassic transition (Wang and Jin, 2000; Yin et al., 2014; Luo et al., 2014, Fig. 1). The Meishan section has been the focus of investigations into the palaeontology and geochemistry of the end-Permian mass extinction for over thirty years (Jin et al., 2000; Yin et al., 1996, 2001; Cao et al., 2009; Xie et al., 2005, 2007; S.Z. Shen et al., 2011; Y.A. Shen et al., 2011; H.J. Song et al., 2013; H.Y. Song et al., 2013; Burgess et al., 2014).

Based on paleontological data, Jin et al. (2000) proposed a sudden mass extinction in the Meishan environment. Subsequent quantitative analyses of fossil occurrences further supported a sudden mass extinction scenario, with the major extinction event occurring during the deposition of the uppermost part of Bed 24e and Bed 25, with some relict Permian taxa surviving until Bed 28 (S.Z. Shen et al., 2011, 2019; Wang et al., 2014). Based on this pattern, Beds 25–28 were identified as a single, continuous extinction interval.

In order to obtain a complete succession of rock samples, and avoid the potential for weathering and surface contamination, two cores were drilled at the Meishan-1 site, 550 m to the west of Meishan Section D. The Meishan-1 core, drilled to a total depth of 214 m, consists of the Lungtan, Changhsing, Yinkeng and Helongshan formations, in ascending order (Cao et al., 2009). Focusing on the interval of the Changhsing Formation immediately preceding the EPME, Beds 21–24

are composed of dark gray, thin- to medium-bedded bioclastic to micritic limestone interbedded with thin-bedded muddy limestone and siliceous mudstone. There is a distinct pyrite lamina at the top of Bed 24e. The contact between the Changhsing and Yinkeng formations is placed at this surface, which represents a transition from limestone to predominantly siliciclastic deposits. Bed 25 is 4-cm-thick, and is composed of illite-montmorillonite ash claystone. Zircons in this ash layer from the outcrop sections at the Meishan quarries have yielded a U-Pb age of 251.941 ± 0.037 Ma (Burgess et al., 2014).

Bed 26 is a 6-cm-thick, black carbonaceous mudstone. Bed 27 can be divided into four layers, labelled as a, b, c and d in ascending order. These are bioclast-bearing packstone and wackestone deposits with an irregular firmground in the middle. The GSSP of the PTB in the Meishan D section has been defined at the base of 27c, marked by the first appearance of *Hindeodus parvus* (Yin et al., 2001). Bed 28 is composed of grayish-green clay, and yields a zircon U-Pb age of 251.880 ± 0.031 Ma (Burgess et al., 2014). Beds 29 and 30 are composed of dark marlstone and calcareous mudstone, respectively. Beds 31 through 34 show an alternation between grayish-green mudstones and marlstones (Beds 32 and 34) and gray claystones of volcanic origin (Beds 31 and 33; Yin et al., 2001; Zheng et al., 2013). Zircons from Bed 33 yield a mean age of 251.583 ± 0.086 Ma (Burgess et al., 2014).

3. Sampling and methods

In this study, we systematically sampled the Meishan-1 core from 114 m (i.e., the upper part of Bed 21, Upper Permian Changhsing Formation) to 100 m (the middle of Bed 34, Lower Triassic Yinkeng Formation) at an average spacing of 2 to 5 cm within Beds 24d-28 and 10 to 30 cm within Beds 21-24c and Beds 29–34. A total of 141 samples were collected. These were broken into pieces (diameter ~2 mm) by hammer, and pieces of the crushed samples were selected to avoid veins and cavities, then further pulverized using a SPEX 8515 Shatterbox with a ceramic puck.

Samples from Beds 21-24d were carbonate rich, and most (49 out of 72) had Fe_T content < 0.5%. Published total organic carbon (TOC) values within these intervals of the core were relatively high, averaging 0.81% (Cao et al., 2009). This combination of low Fe_T content and high TOC values means we cannot safely infer redox conditions based on iron speciation and organic carbon concentrations alone. Additional forms of evidence, such as concentrations of redox-sensitive trace elements like U, V and Mo, benthic macro- and trace fossils, and bioturbation also need to be considered in order to accurately assess redox conditions in the depositional water body (Clarkson et al., 2014; Scholz et al., 2014a, 2014b; Scholz, 2018).

Since carbonate samples where total iron content are < 0.5% usually show spurious iron speciation results, they cannot be interpreted within the established framework of thresholds for recognizing anoxia and euxinia. To address this issue, we selected the 92 samples with Fe_T content > 0.5% for iron speciation analysis. The concentrations of carbonate-associated iron phases (Fe_{carb}), iron oxide-associated phases (Fe_{ox}), and magnetite-associated phases (Fe_{mag}) were analyzed following the procedure of Poulton and Canfield (2005). Fe_{carb}, Fe_{ox}, and Fe_{mag} were measured using a quadrupole Inductively Coupled Plasma Optical Emission Spectrometer (ICP-OES) at the State Key Laboratory of Paleobiology and Stratigraphy, Nanjing Institute of Geology and Palaeontology. Analytical precision was monitored using the GSR-1, GSR-2, and GSR-3 standards, and is better than 5%. Pyrite iron (Fe_{py}) was extracted using the chromium reduction method (Canfield et al., 1986). The Ag_2S-precipitate was weighed to determine the content of pyrite sulfur. Highly reactive iron (Fe_{HR}) was calculated as the sum of Fe_{carb}, Fe_{ox}, Fe_{mag}, and Fe_{py}.

To determine bulk elemental composition, samples were subjected to by multi-acid digestion (HNO_3–HF–HCl) techniques (Kendall et al., 2010; Xiang et al., 2016). After complete dissolution, these solutions were analyzed for the target elements on a quadrupole inductively
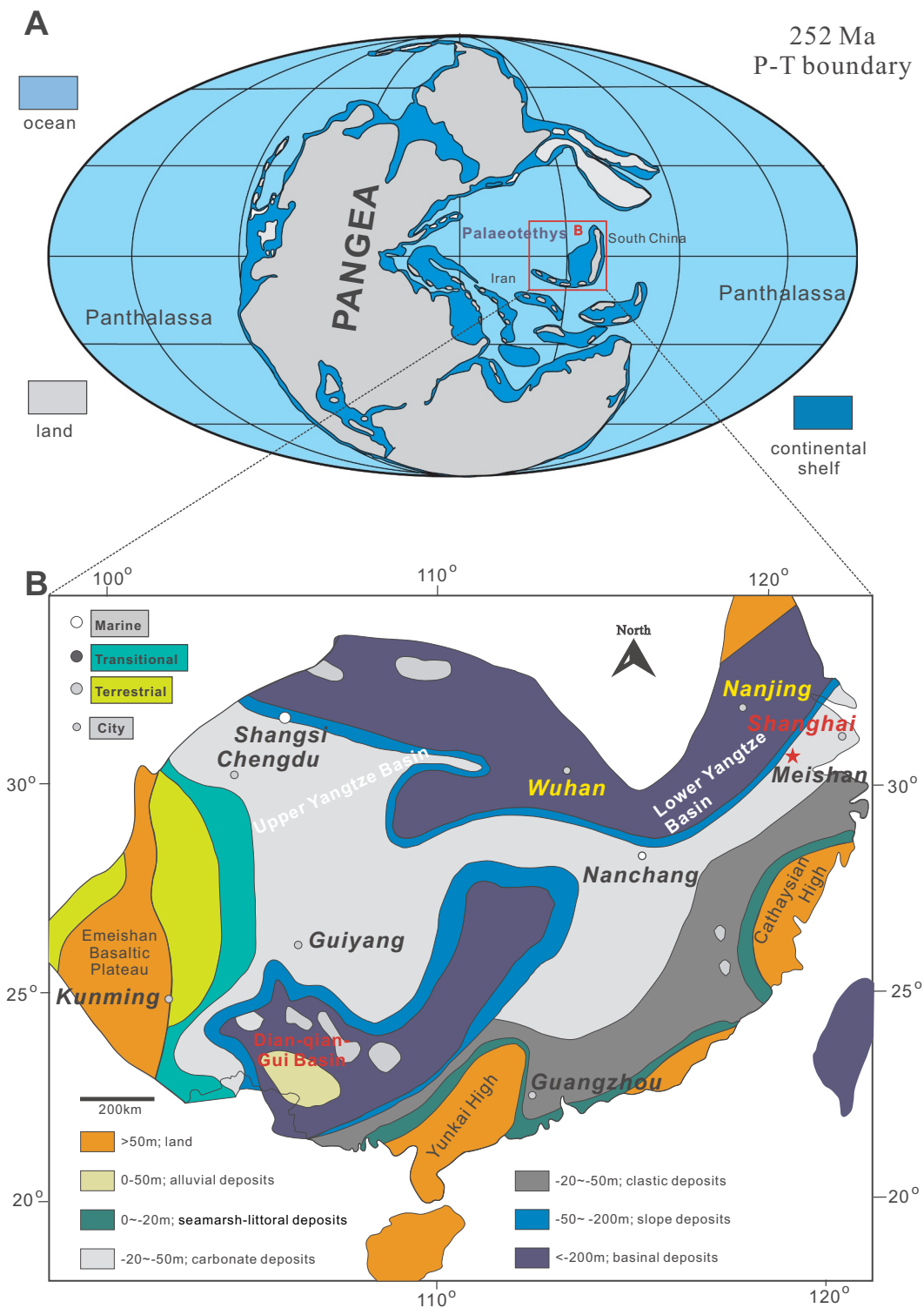
Fig. 1. A) Palaeogeographic map showing the location of the Meishan section on the South China microcontinent, and B) reconstruction of the latest Permian geography of South China, showing the location of the Meishan section (Modified from Wang and Jin, 2000; S.Z. Shen et al., 2011).

coupled plasma mass spectrometer (ICP-MS) and ICP-OES at the Beijing Research Institute of Uranium Geology, China National Nuclear Corporation. The analytical precision, as determined by repeat analysis of the GSR-1, GSR-2, and GSR-3 standards, is better than 5%.

Enrichment factors (X_{EF}; Tribovillard et al., 2006) were calculated as:

$$X_{EF} = (X_{sample}/Al_{sample})/(X_{PAAS}/Al_{PAAS}) \qquad (1)$$

Excess concentrations of trace elements (X_{xs}; Tribovillard et al., 2006) were calculated as:

$$X_{xs} = X_{sample} - Al_{sample} \times (X_{PAAS}/Al_{PAAS}) \qquad (2)$$

where X and Al represent the weight percent concentration of element X and aluminum (Al), respectively. Concentrations are normalized to the value of Post-Archean average Australian shale (PAAS; Taylor and McLennan, 1985). Due to the small differences in trace element

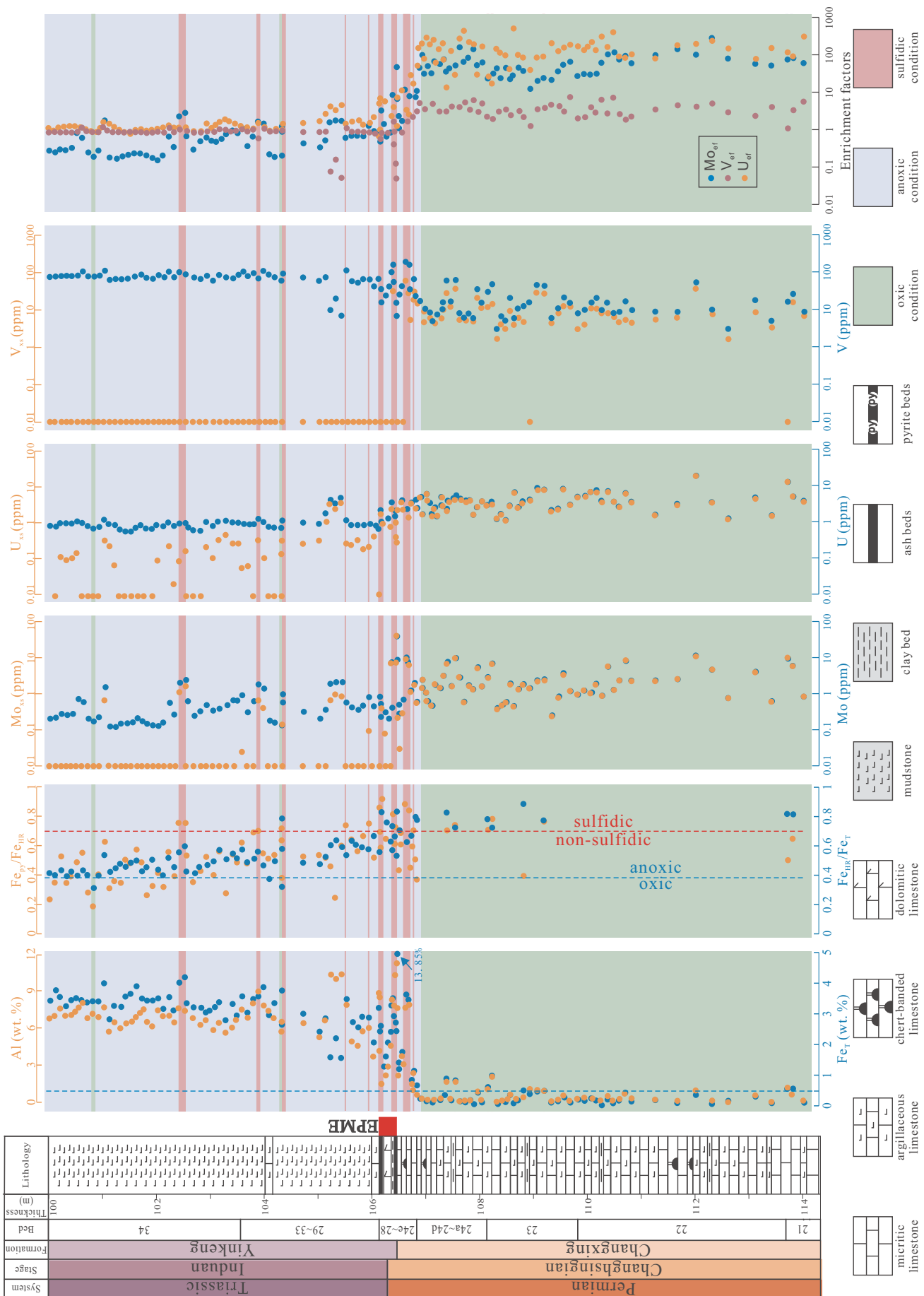**Fig. 2.** Stratigraphic distributions of redox proxies in Beds 21–34 of the Meishan section, including Fe$_T$, Al, Fe$_{HR}$/Fe$_T$, Fe$_{py}$/Fe$_T$, Fe$_{py}$/Fe$_{HR}$ bulk and excess concentrations of Mo, U and V and the enrichment factors for Mo, U and V.

composition between the potential provenance for the Meishan section and PAAS, some samples yielded negative X_{xs} values. As these indicate no substantial authigenic enrichment of element X, we set these negative X_{xs} values to 0.01 for calculating the value of $\log_{10}X_{xs}$ and plots of versus depth.

4. Results

Total aluminum and total iron (Fe_T) content in the Changhsing Formation were generally lower than in the Yinkeng Formation. Fe_T values in the Changhsing Formation vary widely, between 0.05% and 13.85%, with an average value of 0.75%. The maximum value of 13.85% comes from the pyrite laminae in Bed 24e; when this bed is excluded, Fe_T values within the Changhsing Formation are consistently lower than those in the Yinkeng Formation, which range between 1.30% and 4.17%, with an average of 3.10%. Al concentrations in the Changhsing Formation range from 0.07% to 11.15%, with an average of 1.19%, while concentrations in the Yinkeng Formation range between 1.46% and 10.30%, with an average value of 6.69%. Like the Dongpan and Xinmin sections (Shen et al., 2012a), all of the ash beds (Beds 25, 28 and 31) within the Yinkeng Formation at the Meishan section show relatively high Al content, substantially higher than the PAAS value (8.4%, Taylor and McLennan, 1985; Fig. 2, Table S1).

Ratios of Fe_{HR}/Fe_T are generally high in those in samples from Beds 21-24e with Fe_T > 0.5% (*n* = 23), ranging between 0.57 and 0.88 (mean = 0.72). Fe_{HR}/Fe_T ratios in Beds 25–28, which range between 0.53 and 0.83 (mean = 0.67), are higher than those seen in the rest of the Yinkeng Formation. Above these beds, Fe_{HR}/Fe_T ratios in Beds 29–34 range between 0.31 and 0.78 (mean = 0.49) and generally show a decreasing trend up-section (Fig. 2, Table S1). Ratios of Fe_{py}/Fe_{HR} in the 23 measured samples (Fe_T > 0.5%) from Beds 21 to 24e range between 0.37 and 0.87, with an average of 0.65. Ratios of Fe_{py}/Fe_{HR} in Beds 25–28 range between 0.58 and 0.91, with an average of 0.70. Ratios of Fe_{py}/Fe_{HR} in Beds 25–28 are higher than those seen from Bed 29 to Bed 34, which have an average value of 0.49 and decrease systematically upsection (Fig. 2, Table S1).

Maximum concentrations of U, V, and Mo are observed below or during the EPME interval. Maximum U content (19.5 ppm) occurs in the Changhsing Formation (Bed 22, 112 m), while maximum Mo (40 ppm) and V (189 ppm) content appear at 106.46 m and 106.62 m (Bed 24e), respectively. Both U and Mo content below and within the EPME interval are generally higher than PAAS values; above the EPME interval, U and Mo contents are generally lower than PAAS values. The average U content in Beds 21–24, Beds 25–28, and Beds 29–34 is 3.9 ppm, 1.7 ppm, and 1.0 ppm, respectively. Similarly, average Mo content in Beds 21–24, Beds 25–28, and Beds 29–34 is 3.2 ppm, 3.2 ppm, and 0.6 ppm, respectively. Vanadium shows a different stratigraphic pattern than U and Mo content; the average V concentration within Beds 21–24, Beds 25–28, and Beds 29–34 is 25.2 ppm, 50.7 ppm, and 73.4 ppm, respectively. This difference is likely due to the detrital contribution to total V content (Fig. 2, Table S1). Enrichment factors of U, V, and Mo show a gradual decreasing trend from Beds 21–24d, through Beds 24e–28, and into Beds 29–34. Within Beds 21–24d, uranium shows the highest enrichment factors, with an average EF of 144. Vanadium shows only a slight enrichment above PAAS values, with an average EF of 3.5. Enrichment factors of molybdenum are between those of uranium and vanadium, with an average EF of 58.2. Enrichment factors of U, V, and Mo within Beds 24e-28 represent a transitional interval, from enrichment above PAAS values in Beds 21–24 to depletion within Beds 29–34.

5. Discussion

5.1. Evolution of redox conditions around the end-Permian mass extinction event

The ratio of highly reactive iron (Fe_{HR}) to total iron (Fe_T) has been developed as a proxy to differentiate shales deposited under oxygenated

bottom waters from those formed under an anoxic water column, with a threshold value of Fe_{HR}/Fe_T > 0.38 used as the criterion for anoxic conditions (Raiswell and Canfield, 1998; Canfield et al., 2008). Where Fe_{HR}/Fe_T > 0.38, two different types of anoxic conditions can be distinguished using the Fe_{py}/Fe_{HR} ratio. When this ratio shows values > 0.7, it is evidence for deposition in a euxinic water column, with free H_2S, while ratios < 0.7 are consistent with deposition in ferruginous waters, with free dissolved ferrous iron (Poulton and Canfield, 2011; Raiswell et al., 2018). While originally developed for basinal shales, recent studies have found that when total iron content (Fe_T) is > 0.5%, the iron speciation proxy can be applied safely in carbonate-rich sediments (Clarkson et al., 2014). Carbonate-rich samples with low Fe_T content (< 0.5%) and low TOC values (< 0.5%) most likely represent deposition beneath an oxic water column, although additional evidence, such as bioturbation, is required to support this interpretation (Clarkson et al., 2014).

Most samples from Beds 21–24d (49 out of 59) have Fe_T content < 0.5%, which calls into question the value of redox interpretations based on iron speciation (Clarkson et al., 2014). While the high carbonate content and low Al content in Beds 21–24d make enrichment factors unreliable (i.e., often spuriously high regardless of redox conditions), the enrichment factors of Mo are generally lower than those of U in this interval (Figs. 2, 3), indicating that benthic redox conditions did not reach the euxinic threshold, where Mo begins to accumulate more rapidly than U in sediments (Algeo and Tribovillard, 2009). The authigenic U content (U_{xs}) in Beds 21–24d at the Meishan section was between 1.1 ppm and 19.4 ppm, with an average of 4.1 ppm. This is similar to the uranium content of modern carbonate rocks deposited under oxic conditions in the Bahamas, which reaches values as high as 4.7 ppm as a result of U precipitation in sulfidic pore waters (Romaniello et al., 2013). While the average and maximum values of U, V and Mo within Beds 21-24d are consistent with modern oxic settings, they are much lower than the values seen in modern and Holocene hypoxic sediments from the in Baltic Sea (Van Helmond et al., 2018).

These results are consistent with the bottom water during deposition of Beds 21–24d having been generally oxic, without free H_2S (Jin et al., 2000; Yin et al., 2012). Abundant macro- and trace fossils, as well as large and complex burrows (maximum diameter = 9.2 mm), have been found in Beds 21–24d of the Meishan outcrop sections (Fig. 4). The bedding plane bioturbation index reaching values of 4 to 5 in Beds 23–24d, indicating that there was enough dissolved oxygen in the bottom waters to support macrofauna with complex behaviors (Fig. 4, Zhao and Tong, 2010; Chen et al., 2015).

Out of the 59 samples from Beds 21–24d, 10 show Fe_T concentrations > 0.5%, allowing them to be interpreted within the established framework for iron speciation proxies, combined with high Fe_{HR}/Fe_T ratios > 0.38. These samples may indicate deposition under an anoxic water column (Fig. 2). In light of the other evidence for predominantly oxic conditions, we interpret these as short-lived and sporadic anoxic episodes. Multiple-S isotopic evidence also suggests that anoxic watermasses only episodically impinged on the Meishan environment during the deposition of Beds 22–24 (Y.A. Shen et al., 2011).

All samples from Beds 24e–28 show Fe_T content > 0.5%, and Fe_{HR}/Fe_T ratios all exceed the 0.38 threshold, indicating consistently anoxic conditions immediately prior to and during the EPME interval (Figs. 2 and 3). Published elemental geochemistry of conodonts indicates that the volcanic ash beds were deposited under anoxic conditions (Song et al., 2012; Zhao et al., 2013); this is consistent with results from iron speciation, supporting the application of this proxy in volcanic ash deposits despite their distinct mineral and chemical composition and sedimentation rate (Shen et al., 2012b). Moreover, the Fe_{py}/Fe_{HR} ratios of the shale interbeds and pyrite lamina in Bed 24e, the black shale in Bed 26 (106.4 m), and the majority of the carbonates in Bed 27 were > 0.7. This indicates intermittently euxinic conditions during deposition of the EPME horizons (Figs. 2 and 3), with free H_2S expanding out of the porewater system into the lower water column and
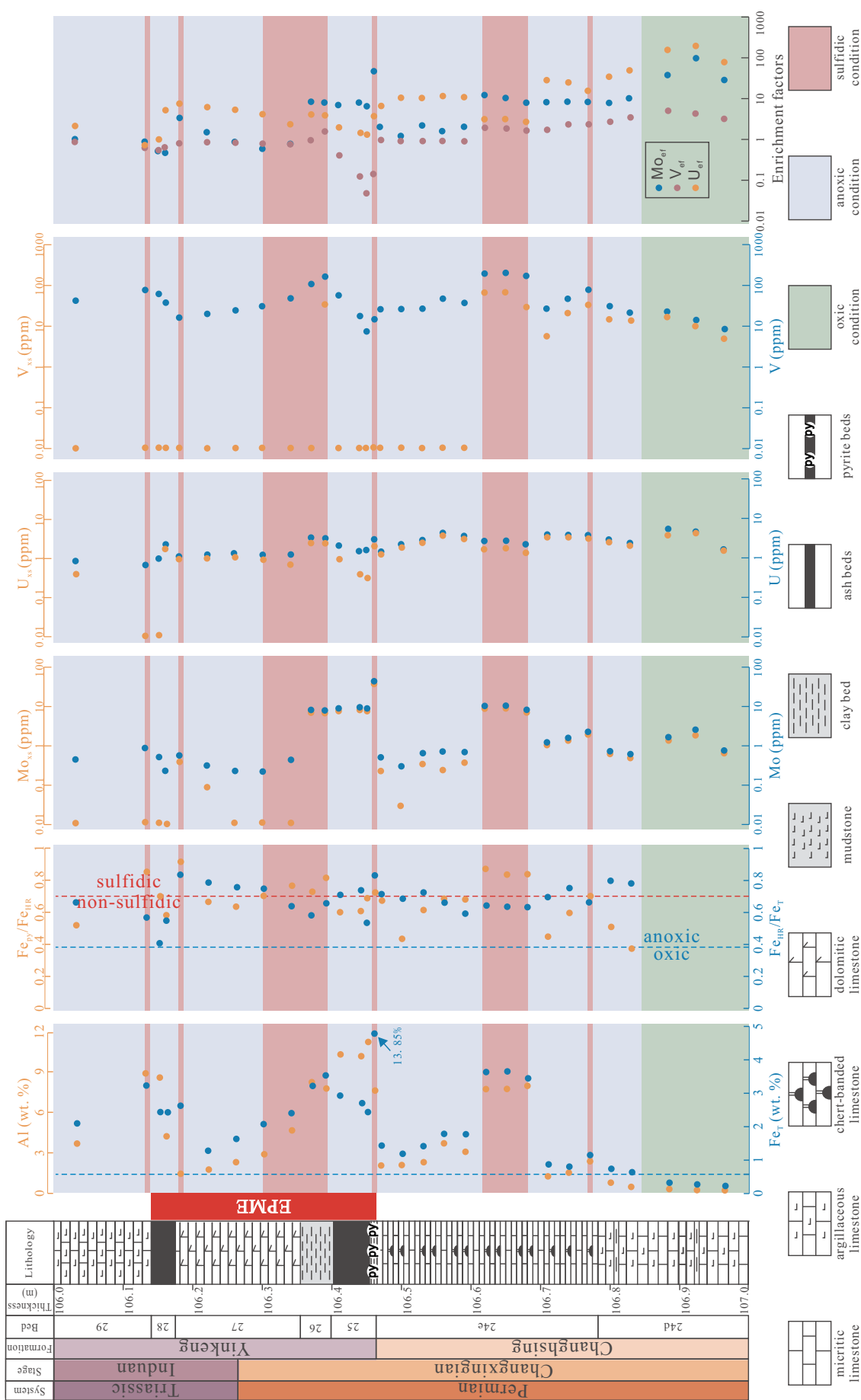
Fig. 3. Expanded plot showing the stratigraphic distributions of redox proxies around the end-Permian mass extinction event horizons (Beds 24d-29) in the Meishan section, including Fe_T, Al, Fe_{HR}/Fe_T, Fe_{py}/Fe_{HR}, the bulk and excess concentrations of Mo, U and V, and the enrichment factors for Mo, U and V.

Fig. 4. Summary of the stratigraphic distributions of the number of species, trace fossil, burrow depth, sea level, Fe_{HR}/Fe_T, Fe_{py}/Fe_{HR}, the enrichment factors for Mo, U and V, TOC, Zinc isotope, and Seawater temperature at the Meishan section. Note: the number of species and sea level data from Yin et al. (2012); Trace fossil and burrow depth data from Zhao and Tong (2010); TOC data from Cao et al. (2009); Zinc isotope data from Liu et al. (2017); Seawater temperature data from Joachimski et al. (2012).

even into the photic zone (Grice et al., 2005; Cao et al., 2009). These euxinic conditions would be favorable for the flourishing of green sulfur bacteria (Grice et al., 2005; Cao et al., 2009), and the formation of syngenetic pyrite framboids (Chen et al., 2015).

The existence of trace fossils within Beds 24e–28, especially the deep burrow within Bed 24e, would seem to contradict our iron speciation results; however, there are two possible explanations for this discrepancy: 1) our samples, typically ~1–2 cm thick, record average conditions over several hundreds or thousands of years (Bond and Wignall, 2010; Burgess et al., 2014). Oscillations in redox potential may have occurred during the interval represented by a single sample. Trace fossils may record much shorter time scales, representing periods of oxia within broader intervals of fluctuating redox conditions, 2), the sampled locality of Zhao and Tong (2010) is hundreds to thousands of meters away from the site of our studied core. The spatial heterogeneity of redox conditions may explain the difference between these two proxies.

Of the 58 samples from Beds 29 to 34, 55 have Fe_{HR}/Fe_T ratios > 0.38, generally showing a decreasing trend up section (Fig. 2). The sedimentation rate may have gradually increased from Bed 29 to Bed 34, due to the increasing flux of terrigenous material (Algeo and Twitchett, 2010). This would have the effect of diluting the authigenic flux of highly reactive iron, resulting in lower Fe_{HR}/Fe_T ratios without bringing them below the threshold indicative of anoxic conditions. Only three samples from Beds 32 and 34 have Fe_{HR}/Fe_T ratios < 0.38, suggesting that transient oxic episodes occurred in the earliest Triassic at Meishan. Seven samples out of 58 in Beds 29 to 34 yielded a combination of Fe_T content > 0.5%, Fe_{HR}/Fe_T ratios > 0.38, and Fe_{py}/Fe_{HR} ratios > 0.70, indicating that they were deposited under euxinic conditions (Fig. 2, Table S1). The remainder of the samples from Beds 29–34 have a combination of Fe_T > 0.5%, Fe_{HR}/Fe_T > 0.38, and Fe_{py}/Fe_{HR} < 0.7, implying ferruginous conditions (Fig. 2).

A ferruginous watermass in the earliest Triassic (Beds 29–34) would favor the loss of fixed nitrogen species (such as NO_3^-) via denitrification and anaerobic ammonium oxidation (anammox), as well as the flourishing of N-fixing cyanobacteria due to the decreasing N:P ratio and higher availability of P and Fe^{2+} (Cao et al., 2009; Luo et al., 2011; Stüeken et al., 2016; Scholz, 2018). These cyanobacteria may have contributed to the development of algal mats that are recorded as laminated sediments in the Early Triassic (Chen et al., 2015).

5.2. Depletion of the oceanic transition metal reservoir

Both the excess fractions and enrichment factors of U, V and Mo indicate that most authigenic precipitation of these three redox sensitive metals occurred prior to the EPME, with minimal authigenic enrichment after the onset of the extinction (Fig. 2). Enrichment factors of U and Mo decline by at least an order of magnitude, with a decrease in the average U_{EF} value from 120 before the EPME to 4 during the EPME. The average Mo_{EF} value declines from 49 before the EPME to 3 during the EPME. Vanadium shows much lower enrichment factors, with an average value of 3.5 in Beds 21–24d, and no apparent authigenic V enrichment after the euxinic interval of Bed 24e (106.62 m to 106.68 m, Figs. 2, 3). This may be a result of the shorter residence time of V in seawater (Tribovillard et al., 2006), meaning that it would have been depleted earlier and more completely than other redox sensitive elements. The decrease in U_{EF}, V_{EF}, and Mo_{EF} may be partially an artifact of increased Al content, corresponding to the lithologic transition from carbonate-dominated to siliciclastic strata at the contact between the Changhsing and Yinkeng formations. However, the excess fractions of these three elements also show a decline between Beds 21–24e and the EPME interval.

Several factors can contribute to the degree of authigenic trace metal enrichment, including oceanic redox conditions, availability of organic host phases, sedimentation rate, and oceanic reservoir size (Tribovillard et al., 2006; Algeo and Lyons, 2006; Algeo and

Tribovillard, 2009). Iron speciation data suggest that Beds 29–34 were generally deposited under more reducing conditions than Beds 21–24d, making it unlikely that the absence of authigenic trace metal precipitation in Beds 29–34 was caused by a more oxygenated environment. The flux of carrier phases, such as organic matter, can also affect authigenic enrichment of redox sensitive elements (Algeo and Lyons, 2006; Algeo and Tribovillard, 2009). Studies of primary productivity around the PTB find that marine productivity decreased sharply across South China (J. Shen et al., 2013), while increasing in many settings across the Panthalassic basin (Algeo et al., 2013). While productivity remains difficult to constrain, the low concentrations of authigenic redox-sensitive trace elements above the EPME is also observed in Japanese pelagic sections (Takahashi et al., 2014), where productivity is likely to have been elevated (Algeo and Twitchett, 2010). This consistent pattern across a range of environments suggests that a decreased flux of organic carrier phases was not the primary driver of decreased trace element enrichment.

Based on U-Pb ages from the Meishan section, the average sediment accumulation rate in Beds 22–24e is ~7 times faster than that in Beds 25–28, and ~4 times faster than that in Beds 29–33 (Burgess et al., 2014). Slow sedimentation rates would reduce the dilution effect of terrestrial siliciclastics and carbonate on the flux of redox-sensitive elements (RSEs). However, the highest excess concentrations and enrichment factors of U, V and Mo do not appear in Beds 25–28, where the slowest sedimentation rates and lowest redox potential would both favor RSE enrichment. Moreover, the stratigraphic pattern of U_{xs} differs from that of V_{xs} and Mo_{xs}; if all were controlled by changes in sedimentation rate, we would expect them to show a similar stratigraphic distribution.

Instead, the principal factors driving the marked difference in authigenic RSE enrichment between pre-EPME, EPME, and post-EPME intervals are likely to be related to the evolution of oceanic U, V and Mo reservoir size (Tribovillard et al., 2006; Piper and Calvert, 2009; Takahashi et al., 2014). Authigenic U precipitation commences within the suboxic zone. The anoxic conditions below the EPME interval would have been favorable for authigenic U precipitation. V (V) is reduced to V (IV) under mildly reducing conditions, and the presence of free H_2S in the watermass causes V(IV) to be further reduced to V(III). Mo is scavenged from solutions under strongly reducing conditions with free H_2S, in the form of organic-thiomolybdate complexes (Zheng et al., 2000). As bottom water redox conditions at Meishan evolved from predominantly oxic with sporadic anoxic conditions in Beds 21–24d, to predominantly ferruginous conditions with intermittently euxinia in Beds 24e–28, seawater U, V, and Mo were successively depleted. The dissolved U reservoir was exhausted first, before the advent of euxinia in Bed 24e. The oceanic V and Mo reservoirs were subsequently exhausted during the periods of more reducing conditions, coinciding with the deposition of Beds 24e–27, and prior to the recurrence of euxinia in Beds 29–34. Our observations of bulk sedimentary U content agree well with conodont Th/U data, which show a rapid increase in Th/U ratios from < 1 to > 78 near Bed 25 (Song et al., 2012). The depletion of U_{xs} under ferruginous conditions during the earliest Triassic is observed across South China, including at the Shangsi section (Xiang et al., 2016).

A depletion of the oceanic V and Mo reservoirs is corroborated by the observation that V_{xs} and Mo_{xs} contents in the euxinic interval of Beds 29–34 are not as high as those in the sulfidic intervals of Beds 24e–28. While lithologic and biomarker evidence suggest that enhanced terrigenous sediment input began at Bed 24 and persisted into Bed 34, U_{xs}, V_{xs}, and Mo_{xs} values at Meishan do not increase in this interval (Xie et al., 2007; Algeo and Twitchett, 2010). While the riverine flux of terrigenous U, V and Mo may have increased, it was not able to keep pace with the enhanced oceanic trace element sink before the deposition of Bed 34.

The use of U concentrations to reconstruct the extent of local or regional seafloor anoxia is complicated in situations where the U

reservoir is depleted to such a degree, However, a nearly synchronous negative shift in $\delta^{238}U$ is observed in sections around the world, including in South China (Brennecka et al., 2011; Lau et al., 2016; Elrick et al., 2017), Turkey (Lau et al., 2016), Japan (Zhang et al., 2018a), and Iran (Zhang et al., 2018b). This isotopic excursion is seen even in oxic environments, suggesting that the expansion of oceanic anoxia was global, affecting both the Paleotethys and Neotethys ocean basins as well as the Panthalassic Ocean. Furthermore, the abrupt increase in Th/U ratios seen prior to the EPME in the Meishan section also appears to be a widespread phenomenon, and is observed in the Dajiang section (Brennecka et al., 2011), in central Saudi Arabia (Clarkson et al., 2013; Eltom et al., 2017), in the Daxiakou section (Elrick et al., 2017), and in the Persian Gulf (Tavakoli and Rahimpour-Bonab, 2012). Our data support the conclusion that the depletion of oceanic U reservoirs around the EPME was a global event, likely related to the enhanced precipitation of U prior to and during the EPME (Ehrenberg et al., 2008; Song et al., 2012; Takahashi et al., 2014; Zhang et al., 2018b).

Although published Mo and V concentrations from EPME sections are not as widely available, authigenic Mo and V data from the Dongpan section in South China (Shen et al., 2012a), the Nhi Tao section in Vietnam (Algeo et al., 2007), the Idrijca Valley section in Western Slovenia (Dolenec et al., 2001), the Rizvanuša section in Croatia (Fio et al., 2010), and the Sverdrup Basin of Arctic Canada (Grasby and Beauchamp, 2009; Grasby et al., 2013, 2016; Proemse et al., 2013), displayed a consistent decreasing trend across the EPME interval. These sections, representing a wide range of lithologies, experienced different sedimentation rates and were deposited over a geographic range of thousands of kilometers. The most probable explanation for the decrease in authigenic Mo and V is the global expansion of anoxic/euxinic watermasses, and the resultant depletion of the oceanic Mo and V reservoir.

There are several potential factors that could have contributed to the expansion of anoxia and euxinia, including a decrease in atmospheric oxygen partial pressure, oceanic stagnation associated with global warming, changes in sea level, or enhanced primary productivity. The relative importance of these factors may have varied between different sections in different regions.

Detailed study on > 20 sections demonstrate that wide-spread End-Permian regression had taken placed in the whole South China (Yin et al., 2014). Some other sections in Pakistan and Italy had also been found the evidences for End-Permian regression (Gall et al., 1998). The End-Permian regression at least is regional, even global. The onset of this global regression coincides with the base of Bed 24e, and a transgressive surface is located at the base of Bed 27 (Yin et al., 2014, Fig. 4). Considering the synchronous negative $\delta^{13}C_{carb}$ shift observed in sections from across both the Paleotethys and Neotethys basins around the PTB (S.Z. Shen et al., 2013), it is possible that the drop in sea level may have caused the formation of a semi-restricted basin at Meishan. This semi-restricted environment would have developed the deposition of Bed 24e and continued until the transgression at the base of Bed 27. As this regression was likely to be a global event (Haq and Schutter, 2008), it would have generated numerous other semi-restricted anoxic/euxinic basins, which could have contributed to the depletion of the oceanic transition metal reservoir.

A slight rise in oceanic temperature within Beds 24–26 relative to underlying Beds 22–23, and the marked warming in sea surface temperature observed at Bed 27 at the Meishan section (Joachimski et al., 2012; Fig. 4). Since anoxia is likely to lag the temperature increase, ocean stagnation as a result of climatic warming may have also contributed to the occurrence of anoxia within Beds 27–34 (Hotinski et al., 2001; Kiehl and Shields, 2005; Song et al., 2019).

Changes in primary productivity may also have played a role in driving anoxia, but interpretation is complicated by conflicting lines of evidence. Back-calculation of organic carbon fluxes based on TOC, phosphorus, and biogenic barium demonstrate that the primary productivity collapsed across South China simultaneously with the EPME

(Algeo et al., 2013; Shen et al., 2013). In contrast, Zn isotope results suggest that primary productivity may have increased within Beds 26–32 (Liu et al., 2017, Fig. 4), which could have stimulated anoxia within the mass extinction interval and earliest Triassic.

5.3. Implications of anoxia and euxinia for the EPME

Anoxia has long been viewed as a potential kill mechanism for the EPME (Isozaki, 1997). The temporal relationship between anoxia and the EPME, and the duration of anoxic conditions, are two key factors governing the potential effect of anoxia on marine fauna (Wignall and Twitchett, 2002; Knoll et al., 2007). Our iron speciation results, in combination with published macro- and trace fossils and bioturbation data from the Meishan outcrop section, indicate that anoxia was only intermittent during deposition of Beds 21–24d, and occurred relatively infrequently. As a result of the primarily oxic conditions, extinction rates did not exceed 33% in any beds of the Changhsing Formation below Bed 24 (Jin et al., 2000). The onset of persistent anoxia occurred at the top of Bed 24d, slightly earlier than the major mass extinction horizon at the base of Bed 25, with an extinction rate of 94% (Jin et al., 2000).

Estimates of anoxic seafloor area around the EPME, based on mass-balance models of $\delta^{238}U$, have suggested that, while the seafloor was never pervasively anoxic, drawdown of aqueous U did occur on a globally significant scale (Elrick et al., 2017; Zhang et al., 2018a, 2018b). The lack of authigenic U and V precipitation under ferruginous conditions at Meishan just prior to and during the EPME supports this interpretation, indicating depletion of the oceanic U and V reservoirs. For this to have occurred, the total volume of anoxic watermasses must have expanded to some extent. This expansion of anoxia, combined with other kill mechanisms such as high surface temperatures (Joachimski et al., 2012; Shen et al., 2019), oceanic acidification (Clarkson et al., 2015; Garbelli et al., 2017), and metal poisoning (Grasby et al., 2011, 2017; Wang et al., 2018) may have contributed to the main pulse of the EPME.

The incursion of euxinic watermasses into the photic zone requires the quantitatively sequestration of oceanic ferrous Fe by H_2S (Raiswell and Canfield, 2012). The intermittently sulfidic conditions at Meishan, and widespread ferruginous conditions in the Neotethys Ocean (Clarkson et al., 2016), suggest that persistent, globally-pervasive euxinia did not occur around the EPME, and was not required to drive the extinction. If this is the case, it is unlikely that the release of H_2S to the atmosphere was sufficient to kill terrestrial vertebrates, or significantly affect the ozone shield (Kump et al., 2005; Harfoot et al., 2008). Euxinia in the Meishan section is mainly confined to Beds 24e–27, corresponding with the complete EPME interval including the principal extinction at the base of Bed 25 (Jin et al., 2000; S.Z. Shen et al., 2011; Yin et al., 2012). Previous models have suggested that if > 6% of global seafloor area became euxinic, oceanic dissolved molybdate would be quantitatively sequestered in sediments (Takahashi et al., 2014). The depletion of the oceanic Mo reservoir during the EPME suggests that euxinic seafloor area exceeded this threshold globally, and may have played an importantly auxiliary role in the marine EPME.

6. Conclusions

At the Meishan GSSP section, the carbonate sediments of Beds 21–24d were deposited under predominantly oxic conditions, punctuated by occasional anoxic events. These conditions were favorable for the flourishing of a diverse marine fauna. As the bottom water evolved toward more persistently anoxic conditions in Beds 24e–28, and the redox potential of the depositional watermass reached the threshold of substantial authigenic trace metal precipitation, U and V concentrations reflect the large-scale regional or global depletion of the dissolved U and V reservoir. Persistent anoxia during the EMPE interval would have killed a substantial proportion of aerobic macrofauna. As the redox

potential decreased further, episodic sulfidic conditions developed, exhausting the oceanic molybdate reservoir, and possibly contributing to decreased primary productivity. Free H_2S in the water-column would have acted as an accomplice of anoxia during the EPME, serving as a proximal macrofauna kill mechanism in some environments.

Supplementary data to this article can be found online at https://doi.org/10.1016/j.palaeo.2020.109626.

Declaration of competing interest

The authors declared that they have no conflicts of interest to this work.

We declare that we do not have any commercial or associative interest that represents a conflict of interest in connection with the submitted work.

Acknowledgements

References

Algeo, T.J., Lyons, T.W., 2006. Mo-total organic carbon covariation in modern anoxic marine environments: implications for analysis of paleoredox and paleohydrographic conditions. Paleoceanography 21, Pa1016.

Algeo, T.J., Tribovillard, N., 2009. Environmental analysis of paleoceanographic systems based on molybdenum-uranium covariation. Chem. Geol. 268, 211–225.

Algeo, T.J., Twitchett, R.J., 2010. Anomalous Early Triassic sediment fluxes due to elevated weathering rates and their biological consequences. Geology 38, 1023–1026.

Algeo, T.J., Ellwood, B., Nguyen, T.K.T., Rowe, H., Maynard, J.B., 2007. The Permian-Triassic boundary at Nhi Tao, Vietnam: evidence for recurrent influx of sulfidic watermasses to a shallow-marine carbonate platform. Paleogeogr. Paleoclimatol. Paleoecol. 252, 304–327.

Algeo, T.J., Henderson, C.M., Tong, J.N., Feng, Q.L., Yin, H.F., Tyson, R.V., 2013. Plankton and productivity during the Permian-Triassic boundary crisis: an analysis of organic carbon fluxes. Glob. Planet. Chang. 105, 52–67.

Basu, A.R., Petaev, M.I., Poreda, R.J., Jacobsen, S.B., Becker, L., 2003. Chondritic meteorite fragments associated with the Permian-Triassic boundary in Antarctica. Science 302, 1388–1392.

Becker, L., Poreda, R.J., Hunt, A.G., Bunch, T.E., Rampino, M., 2001. Impact event at the Permian-Triassic boundary: evidence from extraterrestrial noble gases in fullerenes. Science 291, 1530–1533.

Black, B.A., Lamarque, J.F., Shields, C.A., Elkins-Tanton, L.T., Kiehl, J.T., 2014. Acid rain and ozone depletion from pulsed Siberian Traps magmatism. Geology 42, 67–70.

Black, B.A., Neely, R.R., Lamarque, J.F., Elkins-Tanton, L.T., Kiehl, J.T., Shields, C.A., Mills, M.J., Bardeen, C., 2018. Systemic swings in end-Permian climate from Siberian Traps carbon and sulfur outgassing. Nat. Geosci. 11, 949–954.

Bond, D.P.G., Wignall, P.B., 2010. Pyrite framboid study of marine Permian-Triassic boundary sections: a complex anoxic event and its relationship to contemporaneous mass extinction. Geol. Soc. Am. Bull. 122, 1265–1279.

Brennecka, G.A., Herrmann, A.D., Algeo, T.J., Anbar, A.D., 2011. Rapid expansion of oceanic anoxia immediately before the end-Permian mass extinction. Proc. Natl. Acad. Sci. U. S. A. 108, 17,631–17,634.

Burgess, S.D., Bowring, S.A., 2015. High-precision geochronology confirms voluminous magmatism before, during, and after Earth's most severe extinction. Sci. Adv. 1, e1500470.

Burgess, S.D., Bowring, S., Shen, S.Z., 2014. High-precision timeline for Earth's most severe extinction. Proc. Natl. Acad. Sci. U. S. A. 111, 3316–3321.

Canfield, D.E., Raiswell, R., Westrich, J.T., Reaves, C.M., Berner, R.A., 1986. The use of chromium reduction in the analysis of reduced inorganic sulfur in sediments and shales. Chem. Geol. 54, 149–155.

Canfield, D.E., Poulton, S.W., Knoll, A.H., Narbonne, G.M., Ross, G., Goldberg, T., Strauss, H., 2008. Ferruginous conditions dominated later Neoproterozoic deep water chemistry. Science 321, 949–952.

Cao, C.Q., Love, G.D., Hays, L.E., Wang, W., Shen, S.Z., Summons, R.E., 2009. Biogeochemical evidence for euxinic oceans and ecological disturbance presaging the end-Permian mass extinction event. Earth Planet. Sci. Lett. 281, 188–201.

Chen, J., Shen, S.Z., Li, X.H., Xu, Y.G., Joachimski, M.M., Bowring, S.A., Erwin, D.H.,

Yuan, D.X., Chen, B., Zhang, H., Wang, Y., Cao, C.Q., Zheng, Q.F., Mu, L., 2016. High-resolution SIMS oxygen isotope analysis on conodont apatite from South China and implications for the end-Permian mass extinction. Paleogeogr. Paleoclimatol. Paleoecol. 448, 26–38.

Chen, Z.Q., Yang, H., Luo, M., Benton, M.J., Kaiho, K., Zhao, L.S., Huang, Y.G., Zhang, K.X., Fang, Y.H., Jiang, H.S., Qiu, H., Li, Y., Tu, C.Y., Shi, L., Zhang, L., Feng, X.Q., Chen, L., 2015. Complete biotic and sedimentary records of the Permian–Triassic transition from Meishan section, South China: ecologically assessing mass extinction and its aftermath. Earth-Sci. Rev. 149, 67–107.

Clarkson, M.O., Richoz, S., Wood, R.A., Maurer, F., Krystyn, L., McGurty, D.J., Astratti, D., 2013. A new high-resolution $\delta^{13}C$ record for the Early Triassic: insights from the Arabian Platform. Gondwana Res 24, 233–242.

Clarkson, M.O., Poulton, S.W., Guilbaud, R., Wood, R.A., 2014. Assessing the utility of Fe/Al and Fe-speciation to record water column redox conditions in carbonate-rich sediments. Chem. Geol. 382, 111–122.

Clarkson, M.O., Kasemann, S.A., Wood, R.A., Lenton, T.M., Daines, S.J., Richoz, S., Ohnemueller, F., Meixner, A., Poulton, S.W., Tipper, E.T., 2015. Ocean acidification and the Permo-Triassic mass extinction. Science 348, 229–232.

Clarkson, M.O., Wood, R.A., Poulton, S.W., Richoz, S., Newton, R.J., Kasemann, S.A., Bowyer, F., Krystyn, L., 2016. Dynamic anoxic ferruginous conditions during the end-Permian mass extinction and recovery. Nat. Commun. 7, 12236.

Courtillot, V.E., Renne, P.R., 2003. On the ages of flood basalt events. C. R. Geosci. 335, 113–140.

Dolenec, T., Lojen, S., Ramovs, A., 2001. The Permian-Triassic boundary in Western Slovenia (Idrijca Valley section): magnetostratigraphy, stable isotopes, and elemental variations. Chem. Geol. 175, 175–190.

Ehrenberg, S.N., Svana, T.A., Swart, P.K., 2008. Uranium depletion across the Pennian-Triassic boundary in Middle East carbonates: signature of oceanic anoxia. AAPG Bull 92, 691–707.

Elrick, M., Polyak, V., Algeo, T.J., Romaniello, S., Asmerom, Y., Herrmann, A.D., Anbar, A.D., Zhao, L.S., Chen, Z.Q., 2017. Global-ocean redox variation during the middle-late Permian through Early Triassic based on uranium isotope and Th/U trends of marine carbonates. Geology 45, 163–166.

Eltom, H.A., Abdullatif, O.M., Babalola, L.O., 2017. Redox conditions through the Permian-Triassic transition in the upper Khuff formation, Saudi Arabia. Paleogeogr. Paleoclimatol. Paleoecol. 472, 203–215.

Fio, K., Spangenberg, J.E., Vlahovic, I., Sremac, J., Velic, I., Mrinjek, E., 2010. Stable isotope and trace element stratigraphy across the Permian-Triassic transition: a redefinition of the boundary in the Velebit Mountain, Croatia. Chem. Geol. 278, 38–57.

Gall, J.C., Grauvogel-Stamm, L., Nel, A., Papier, F., 1998. The Permian mass extinction and the Triassic recovery. Comptes Rendus Acad. Sci. Ser II-A 326, 1–12.

Garbelli, C., Angiolini, L., Shen, S.Z., 2017. Biomineralization and global change: a new perspective for understanding the end-Permian extinction. Geology 45, 19–22.

Grasby, S.E., Beauchamp, B., 2009. Latest Permian to Early Triassic basin-to-shelf anoxia in the Sverdrup Basin, Arctic Canada. Chem. Geol. 264, 232–246.

Grasby, S.E., Sanei, H., Beauchamp, B., 2011. Catastrophic dispersal of coal fly ash into oceans during the latest Permian extinction. Nat. Geosci. 4, 104–107.

Grasby, S.E., Beauchamp, B., Embry, A., Sanei, H., 2013. Recurrent Early Triassic ocean anoxia. Geology 41, 175–178.

Grasby, S.E., Beauchamp, B., Knies, J., 2016. Early Triassic productivity crises delayed recovery from world's worst mass extinction. Geology 44, 779–782.

Grasby, S.E., Shen, W.J., Yin, R.S., Gleason, J.D., Blum, J.D., Lepak, R.F., Hurley, J.P., Beauchamp, B., 2017. Isotopic signatures of mercury contamination in latest Permian oceans. Geology 45, 55–58.

Grice, K., Cao, C.Q., Love, G.D., Bottcher, M.E., Twitchett, R.J., Grosjean, E., Summons, R.E., Turgeon, S.C., Dunning, W., Jin, Y.G., 2005. Photic zone euxinia during the Permian-Triassic superanoxic event. Science 307, 706–709.

Haq, B.U., Schutter, S.R., 2008. A chronology of Paleozoic sea-level changes. Science 322, 64–68.

Harfoot, M.B., Pyle, J.A., Beerling, D.J., 2008. End-Permian ozone shield unaffected by oceanic hydrogen sulphide and methane releases. Nat. Geosci. 1, 247–252.

Hinojosa, J.L., Brown, S.T., Chen, J., DePaolo, D.J., Paytan, A., Shen, S.Z., Payne, J.L., 2012. Evidence for end-Permian ocean acidification from calcium isotopes in biogenic apatite. Geology 40, 743–746.

Hotinski, R.M., Bice, K.L., Kump, L.R., Najjar, R.G., Arthur, M.A., 2001. Ocean stagnation and end-Permian anoxia. Geology 29, 7–10.

Huey, R.B., Ward, P.D., 2005. Hypoxia, global warming, and terrestrial Late Permian extinctions. Science 308, 398–401.

Isozaki, Y., 1997. Permo-Triassic boundary superanoxia and stratified superocean: records from lost deep sea. Science 276, 235–238.

Jin, Y.G., Wang, Y., Wang, W., Shang, Q.H., Cao, C.Q., Erwin, D.H., 2000. Pattern of marine mass extinction near the Permian-Triassic boundary in South China. Science 289, 432–436.

Joachimski, M.M., Lai, X.L., Shen, S.Z., Jiang, H.S., Luo, G.M., Chen, B., Chen, J., Sun, Y.D., 2012. Climate warming in the latest Permian and the Permian-Triassic mass extinction. Geology 40, 195–198.

Kendall, B., Reinhard, C.T., Lyons, T.W., 2010. Pervasive oxygenation along late Archaean ocean margins. Nat. Geosci. 3, 647–652.

Kiehl, J.T., Shields, C.A., 2005. Climate simulation of the latest Permian: implications for mass extinction. Geology 33, 757–760.

Knoll, A.H., Bambach, R.K., Payne, J.L., Pruss, S., Fischer, W.W., 2007. Paleophysiology and end-Permian mass extinction. Earth Planet. Sci. Lett. 256, 295–313.

Kump, L.R., Pavlov, A., Arthur, M., 2005. Massive release of hydrogen sulfide to the surface ocean and atmosphere during intervals of oceanic anoxia. Geology 33, 397–400.

Lau, K.V., Maher, K., Altiner, D., Kelley, B.M., Kump, L.R., Lehrmann, D.J., Silva-Tamayo,

J.C., Weaver, K.L., Yu, M.Y., Payne, J.L., 2016. Marine anoxia and delayed Earth system recovery after the end-Permian extinction. Proc. Natl. Acad. Sci. U. S. A. 113, 2360–2365.

Liu, S.A., Wu, H.C., Shen, S.Z., Jiang, G.Q., Zhang, S.H., Lv, Y.W., Zhang, H., Li, S.G., 2017. Zinc isotope evidence for intensive magmatism immediately before the end-Permian mass extinction. Geology 45, 343–346.

Luo, G.M., Kump, L.R., Wang, Y.B., Tong, J.N., Arthur, M.A., Yang, H., Huang, J.H., Yin, H.F., Xie, S.C., 2010. Isotopic evidence for an anomalously low oceanic sulfate concentration following end-Permian mass extinction. Earth Planet. Sci. Lett. 300, 101–111.

Luo, G.M., Wang, Y.B., Algeo, T.J., Kump, L.R., Bai, X., Yang, H., Yao, L., Xie, S.C., 2011. Enhanced nitrogen fixation in the immediate aftermath of the latest Permian marine mass extinction. Geology 39, 647–650.

Luo, G.M., Algeo, T.J., Huang, J.H., Zhou, W.F., Wang, Y.B., Yang, H., Richoz, S., Xie, S.C., 2014. Vertical δ13Corg gradients record changes in planktonic microbial community composition during the end-Permian mass extinction. Palaeogeogr. Palaeoclimatol. Palaeoecol. 396, 119–131.

Mettam, C., Zerkle, A.L., Claire, M.W., Izon, G., Junium, C.J., Twitchett, R.J., 2017. High-frequency fluctuations in redox conditions during the latest Permian mass extinction. Paleogeogr. Paleoclimatol. Paleoecol. 485, 210–223.

Newton, R.J., Pevitt, E.L., Wignall, P.B., Bottrell, S.H., 2004. Large shifts in the isotopic composition of seawater sulphate across the Permo-Triassic boundary in northern Italy. Earth Planet. Sci. Lett. 218, 331–345.

Payne, J.L., Turchyn, A.V., Paytan, A., DePaolo, D.J., Lehrmann, D.J., Yu, M.Y., Wei, J.Y., 2010. Calcium isotope constraints on the end-Permian mass extinction. Proc. Natl. Acad. Sci. U. S. A. 107, 8543–8548.

Penn, J.L., Deutsch, C., Payne, J.L., Sperling, E.A., 2018. Temperature-dependent hypoxia explains biogeography and severity of end-Permian marine mass extinction. Science 362, eaat1327.

Piper, D.Z., Calvert, S.E., 2009. A marine biogeochemical perspective on black shale deposition. Earth Sci. Rev. 95, 63–96.

Poulton, S.W., Canfield, D.E., 2005. Development of a sequential extraction procedure for iron: implications for iron partitioning in continentally derived particulates. Chem. Geol. 214, 209–221.

Poulton, S.W., Canfield, D.E., 2011. Ferruginous conditions: a dominant feature of the ocean through earth's history. Elements 7, 107–112.

Proemse, B.C., Grasby, S.E., Wieser, M.E., Mayer, B., Beauchamp, B., 2013. Molybdenum isotopic evidence for oxic marine conditions during the latest Permian extinction. Geology 41, 967–970.

Raiswell, R., Canfield, D.E., 1998. Sources of iron for pyrite formation in marine sediments. Am. J. Sci. 298, 219–245.

Raiswell, R., Canfield, D.E., 2012. The iron biogeochemical cycle past and present. Geochem. Perspect. 1, 1–220.

Raiswell, R., Hardisty, D.S., Lyons, T.W., Canfield, D.E., Owens, J.D., Planavsky, N.J., Poulton, S.W., Reinhard, C.T., 2018. The iron paleoredox proxies: a guide to the pitfalls, problems and proper practice. Am. J. Sci. 318, 491–526.

Romaniello, S.J., Herrmann, A.D., Anbar, A.D., 2013. Uranium concentrations and 238U/235U isotope ratios in modern carbonates from the Bahamas: assessing a novel paleoredox proxy. Chem. Geol. 362, 305–316.

Scholz, F., 2018. Identifying oxygen minimum zone-type biogeochemical cycling in Earth history using inorganic geochemical proxies. Earth-Sci. Rev. 184, 29–45.

Scholz, F., Severmann, S., McManus, J., Noffke, A., Lomnitz, U., Hensen, C., 2014a. On the isotope composition of reactive iron in marine sediments: redox shuttle versus early diagenesis. Chem. Geol. 389, 48–59.

Scholz, F., Severmann, S., McManus, J., Hensen, C., 2014b. Beyond the Black Sea paradigm: the sedimentary fingerprint of an open-marine iron shuttle. Geochim. Cosmochim. Acta 127, 368–380.

Sepkoski, J.J., 1984. A kinetic-model of Phanerozoic taxonomic diversity .3. post-Paleozoic families and mass extinctions. Paleobiology 10, 246–267.

Shen, J., Algeo, T.J., Zhou, L., Feng, Q., Yu, J., Ellwood, B., 2012a. Volcanic perturbations of the marine environment in South China preceding the latest Permian mass extinction and their biotic effects. Geobiology 10, 82–103.

Shen, J., Algeo, T.J., Hu, Q., Zhang, N., Zhou, L., Xia, W.C., Xie, S.C., Feng, Q.L., 2012b. Negative C-isotope excursions at the Permian-Triassic boundary linked to volcanism. Geology 40, 963–966.

Shen, J., Algeo, T.J., Feng, Q.L., Zhou, L., Feng, L.P., Zhang, N., Huang, J.H., 2013. Volcanically induced environmental change at the Permian-Triassic boundary (Xiakou, Hubei Province, South China): related to West Siberian coal-field methane releases? J. Asian Earth Sci. 75, 95–109.

Shen, S.Z., Crowley, J.L., Wang, Y., Bowring, S.A., Erwin, D.H., Sadler, P.M., Cao, C.Q., Rothman, D.H., Henderson, C.M., Ramezani, J., Zhang, H., Shen, Y'.A., Wang, X.D., Wang, W., Mu, L., Li, W.Z., Tang, Y.G., Liu, X.L., Liu, L.L., Zeng, Y., Jiang, Y.F., Jin, Y.G., 2011. Calibrating the end-Permian mass extinction. Science 334, 1367–1372.

Shen, S.Z., Cao, C.Q., Zhang, H., Bowring, S.A., Henderson, C.M., Payne, J.L., Davydov, V.I., Chen, B., Yuan, D.X., Zhang, Y.C., Wang, W., Zheng, Q.F., 2013. High-resolution δ13Ccarb chemostratigraphy from latest Guadalupian through earliest Triassic in South China and Iran. Earth Planet. Sci. Lett. 375, 156–165.

Shen, S.Z., Ramezani, J., Chen, J., Cao, C.Q., Erwin, D.H., Zhang, H., Xiang, L., Schoepfer, S.D., Henderson, C.M., Zheng, Q.F., Bowring, S.A., Wang, Y., Li, X.H., Wang, X.D., Yuan, D.X., Zhang, Y.C., Mu, L., Wang, J., Wu, Y.S., 2019. A sudden end-Permian mass extinction in South China. Geol. Soc. Am. Bull. 131, 205–223.

Shen, W.J., Sun, Y.G., Lin, Y.T., Liu, D.H., Chai, P.X., 2011. Evidence for wildfire in Meishan section and implications for Permian-Triassic events. Geochim. Cosmochim. Acta 75, 1992–2006.

Shen, Y.A., Farquhar, J., Zhang, H., Masterson, A., Zhang, T.G., Wing, B.A., 2011. Multiple S-isotopic evidence for episodic shoaling of anoxic water during Late

Permian mass extinction. Nat. Commun. 2, 210–214.

Sobolev, S.V., Sobolev, A.V., Kuzmin, D.V., Krivolutskaya, N.A., Petrunin, A.G., Arndt, N.T., Radko, V.A., Vasiliev, Y.R., 2011. Linking mantle plumes, large igneous provinces and environmental catastrophes. Nature 477, 312–316.

Song, H.J., Wignall, P.B., Tong, J.N., Bond, D.P.G., Song, H.Y., Lai, X.L., Zhang, K.X., Wang, H.M., Chen, Y.L., 2012. Geochemical evidence from bio-apatite for multiple oceanic anoxic events during Permian-Triassic transition and the link with end-Permian extinction and recovery. Earth Planet. Sci. Lett. 353, 12–21.

Song, H.J., Wignall, P.B., Tong, J.N., Yin, H.F., 2013. Two pulses of extinction during the Permian-Triassic crisis. Nat. Geosci. 6, 52–56.

Song, H.J., Wignall, P.B., Chu, D.L., Tong, J.N., Sun, Y.D., Song, H.Y., He, W.H., Tian, L., 2014. Anoxia/high temperature double whammy during the Permian-Triassic marine crisis and its aftermath. Sci. Rep. 4, 4132.

Song, H.J., Wignall, P.B., Tong, J.N., Song, H.Y., Chen, J., Chu, D.L., Tian, L., Luo, M., Zong, K.Q., Chen, Y.L., Lai, X.L., Zhang, K.X., Wang, H.M., 2015. Integrated Sr isotope variations and global environmental changes through the Late Permian to early Late Triassic. Earth Planet. Sci. Lett. 424, 140–147.

Song, H.Y., Tong, J.N., Algeo, T.J., Horacek, M., Qiu, H.O., Song, H.J., Tian, L., Chen, Z.Q., 2013. Large vertical δ13CDIC gradients in Early Triassic seas of the South China craton: implications for oceanographic changes related to Siberian Traps volcanism. Glob. Planet. Change 105, 7–20.

Song, H.Y., Tong, J.N., Tian, L., Song, H.J., Qiu, H.O., Zhu, Y.Y., Algeo, T., 2014a. Paleoredox conditions across the Permian-Triassic boundary in shallow carbonate platform of the Nanpanjiang Basin, South China. Sci. China-Earth Sci. 57, 1030–1038.

Song, H.Y., Tong, J.N., Algeo, T.J., Song, H.J., Qiu, H.O., Zhu, Y.Y., Tian, L., Bates, S., Lyons, T.W., Luo, G.M., Kump, L.R., 2014b. Early Triassic seawater sulfate drawdown. Geochim. Cosmochim. Acta 128, 95–113.

Song, H.Y., Du, Y., Algeo, T.J., Tong, J.N., Owens, J.D., Song, H.J., Tian, L., Qiu, H., Zhu, Y.Y., Lyons, T.W., 2019. Cooling-driven oceanic anoxia across the Smithian/Spathian boundary (mid-Early Triassic). Earth-Sci. Rev. 195, 133–146.

Stanley, S.M., 2016. Estimates of the magnitudes of major marine mass extinctions in earth history. Proc. Natl. Acad. Sci. U. S. A. 113, E6325–E6334.

Stüeken, E.E., Kipp, M.A., Koehler, M.C., Buick, R., 2016. The evolution of Earth's biogeochemical nitrogen cycle. Earth-Sci. Rev. 160, 220–239.

Sun, H., Xiao, Y.L., Gao, Y.J., Zhang, G.J., Casey, J.F., Shen, Y.A., 2018. Rapid enhancement of chemical weathering recorded by extremely light seawater lithium isotopes at the Permian-Triassic boundary. Proc. Natl. Acad. Sci. U. S. A. 115, 3782–3787.

Sun, Y.D., Joachimski, M.M., Wignall, P.B., Yan, C.B., Chen, Y.L., Jiang, H.S., Wang, L.N., Lai, X.L., 2012. Lethally hot temperatures during the Early Triassic greenhouse. Science 338, 366–370.

Takahashi, S., Yamasaki, S., Ogawa, Y., Kimura, K., Kaiho, K., Yoshida, T., Tsuchiya, N., 2014. Bioessential element-depleted ocean following the euxinic maximum of the end-Permian mass extinction. Earth Planet. Sci. Lett. 393, 94–104.

Tavakoli, V., Rahimpour-Bonab, H., 2012. Uranium depletion across Permian-Triassic boundary in Persian Gulf and its implications for paleooceanic conditions. Paleogeogr. Paleoclimatol. Paleoecol. 350, 101–113.

Taylor, S.R., McLennan, S.M., 1985. The Continental Crust: Its Composition and Evolution. Blackwell, Malden, Mass, pp. 1–312.

Tian, L., Tong, J.N., Xiao, Y.F., Benton, M.J., Song, H.Y., Song, H.J., Liang, L., Wu, K., Chu, D.L., Algeo, T.J., 2019. Environmental instability prior to end-Permian mass extinction reflected in biotic and facies changes on shallow carbonate platforms of the Nanpanjiang Basin (South China). Paleogeogr. Paleoclimatol. Paleoecol. 519, 23–36.

Tribovillard, N., Algeo, T.J., Lyons, T., Riboulleau, A., 2006. Trace metals as paleoredox and paleoproductivity proxies: an update. Chem. Geol. 232, 12–32.

Van Helmond, N.A.G.M., Jilbert, T., Slomp, C.P., 2018. Hypoxia in the Holocene Baltic Sea: comparing modern versus past intervals using sedimentary trace metals. Chem. Geol. 493, 478–490.

Wang, X.D., Cawood, P.A., Zhao, H., Zhao, L.S., Grasby, S.E., Chen, Z.Q., Wignall, P.B., Lv, Z.Y., Han, C., 2018. Mercury anomalies across the end Permian mass extinction in South China from shallow and deep water depositional environments. Earth Planet. Sci. Lett. 496, 159–167.

Wang, Y., Jin, Y.G., 2000. Permian palaeogeographic evolution of the Jiangnan Basin, South China. Palaeogeogr. Palaeoclimatol. Palaeoecol. 160, 35–44.

Wang, Y., Sadler, P.M., Shen, S.Z., Erwin, D.H., Zhang, Y.C., Wang, X.D., Wang, W., Crowley, J.L., Henderson, C.M., 2014. Quantifying the process and abruptness of the end-Permian mass extinction. Paleobiology 40, 113–129.

Wignall, P.B., Twitchett, R.J., 1996. Oceanic anoxia and the end Permian mass extinction. Science 272, 1155–1158.

Wignall, P.B., Twitchett, R.J., 2002. Extent, duration, and nature of the Permian-Triassic superanoxic event. In: Koeberl, C., MacLeod, K.G. (Eds.), Catastrophic Events and Mass Extinctions: Impacts and Beyond. Geol. Soc. Am. Special Paper 356pp. 395–413.

Xiang, L., Schoepfer, S.D., Zhang, H., Yuan, D.X., Cao, C.Q., Zheng, Q.F., Henderson, C.M., Shen, S.Z., 2016. Oceanic redox evolution across the end-Permian mass extinction at Shangsi, South China. Paleoclimatol. Paleoecol. 448, 59–71.

Xie, S.C., Pancost, R.D., Yin, H.F., Wang, H.M., Evershed, R.P., 2005. Two episodes of microbial change coupled with Permo/Triassic faunal mass extinction. Nature 434, 494–497.

Xie, S.C., Pancost, R.D., Huang, J.H., Wignall, P.B., Yu, J.X., Tang, X.Y., Chen, L., Huang, X.Y., Lai, X.L., 2007. Changes in the global carbon cycle occurred as two episodes during the Permian-Triassic crisis. Geology 35, 1083–1086.

Yin, H., Sweet, W.C., Glenister, B.F., Kotlyar, G., Kozur, H., Newell, N.D., Sheng, J., Yang, Z., Zakharov, Y.D., 1996. Recommendation of the Meishan section as global stratotype section and point for basal boundary of Triassic System. Newsl. Stratigr. 34, 81–108.

Yin, H.F., Zhang, K.X., Tong, J.N., Yang, Z.Y., Wu, S.B., 2001. The global stratotype

section and point (GSSP) of the Permian-Triassic boundary. Episodes 24, 102–114.

Yin, H.F., Xie, S.C., Luo, G.M., Algeo, T.J., Zhang, K.X., 2012. Two episodes of environmental change at the Permian-Triassic boundary of the GSSP section Meishan. Earth-Sci. Rev. 115, 163–172.

Yin, H.F., Jiang, H.S., Xia, W.C., Feng, Q.L., Zhang, N., Shen, J., 2014. The end-Permian regression in South China and its implication on mass extinction. Earth Sci. Rev. 137, 19–33.

Zhang, F.F., Algeo, T.J., Romaniello, S.J., Cui, Y., Zhao, L.S., Chen, Z.Q., Anbar, A.D., 2018a. Congruent Permian-Triassic δ^{238}U records at Panthalassic and Tethyan sites: confirmation of global-oceanic anoxia and validation of the U-isotope paleoredox proxy. Geology 46, 327–330.

Zhang, F.F., Romaniello, S.J., Algeo, T.J., Lau, K.V., Clapham, M.E., Richoz, S., Herrmann, A.D., Smith, H., Horacek, M., Anbar, A.D., 2018b. Multiple episodes of extensive marine anoxia linked to global warming and continental weathering following the latest Permian mass extinction. Sci. Adv. 4, e1602921.

Zhao, L.S., Chen, Z.Q., Algeo, T.J., Chen, J.B., Chen, Y.L., Tong, J.N., Gao, S., Zhou, L., Hu, Z.C., Liu, Y.S., 2013. Rare-earth element patterns in conodont albid crowns: evidence for massive inputs of volcanic ash during the latest Permian biocrisis? Glob. Planet. Change 105, 135–151.

Zhao, X.M., Tong, J.N., 2010. Two episodic changes of trace fossils through the Permian-Triassic transition in the Meishan cores, Zhejiang Province. Sci. China-Earth Sci. 53, 1885–1893.

Zheng, Q.F., Cao, C.Q., Zhang, M.Y., 2013. Sedimentary features of the Permian-Triassic boundary sequence of the Meishan section in Changxing County, Zhejiang Province. Sci. China-Earth Sci. 56, 956–969.

Zheng, Y., Anderson, R.F., Van Geen, A., Kuwabara, J., 2000. Authigenic molybdenum formation in marine sediments: a link to pore water sulfide in the Santa Barbara Basin. Geochim. Cosmochim. Acta 64, 4165–4178.